**Supporting Information**

# Oxide Defect Engineering Enables to Couple Solar Energy into Oxygen Activation

**Ning Zhang†, Xiyu Li†, Huacheng Ye, Shuangming Chen, Huanxin Ju, Daobin Liu, Yue Lin, Wei Ye, Chengming Wang, Qian Xu, Junfa Zhu, Li Song, Jun Jiang*, and Yujie Xiong***

*Hefei National Laboratory for Physical Sciences at the Microscale, iChEM (Collaborative Innovation Center of Chemistry for Energy Materials), School of Chemistry and Materials Science, Hefei Science Center (CAS), and National Synchrotron Radiation Laboratory, University of Science and Technology of China, Hefei, Anhui 230026, P. R. China*

**Corresponding author. E-mail: yjxiong@ustc.edu.cn; jiangj1@ustc.edu.cn*

†These authors contributed equally.

## 1. Experimental Procedure:

**Materials.** Sodium tungstate dehydrate ($Na_2WO_4 \cdot 2H_2O$, 99.5%) and commercial $WO_3$ (99.9 % metal basis) were purchased from Aladdin. Citric acid (CA, > 99.5%) and 5,5-dimethyl-1-pyrroline *N*-oxide (DMPO, for ESR spectroscopy) were purchased from Sigma-Aldrich. D(+)-Glucose (AR), hydrochloric acid (36~38%, AR), anhydrous ethanol (EtOH, AR), ethyl acetate (EtOAc, AR) and acetonitrile ($CH_3CN$, AR) were obtained from Sinopharm Chemical Reagent Co., Ltd. All amines for light-driven catalytic experiments were obtained from Energy Chemical. The water used in all experiments was de-ionized (DI). All of the chemical reagents of analytical grade were used as received without further purification.

**Preparation of precursor $WO_3 \cdot H_2O$ nanosheets.** $WO_3 \cdot H_2O$ nanosheets were prepared by a mild hydrothermal method. Briefly, 1 mmol of $Na_2WO_4 \cdot 2H_2O$ was initially added into 30 mL of $H_2O$ to prepare a transparent solution, into which 1.5 mmol of citric acid and 5 mmol of glucose were then added in order. After vigorous stirring for 10 min, 3 mL of HCl solution (6 M) was added into the mixed solution, followed by another 30-min stirring. The mixture was transferred into a 50-mL Teflon-lined autoclave, which was then sealed and heated at 393 K for 24 h. After the autoclave had cooled down to room temperature, the resultant product was separated by centrifugation, washed with water and anhydrous ethanol for several times until the organics were completely removed. Finally the product was dried at 333 K in vacuum oven for 24 h for further use and characterization.

## 2. Sample characterizations:

Prior to electron microscopy characterizations, a drop of the aqueous suspension of particles was placed on a piece of silicon wafer or carbon-coated copper grid and dried under ambient conditions. SEM images were taken on a FEI Sirion-200 field emission scanning electron microscope operated at 5 kV. TEM images were taken on a JEOL JEM-2100F field-emission high-resolution transmission electron microscope operated

at 200 kV. HAADF-STEM images were collected on a JEOL ARM-200F field-emission transmission electron microscope operated at 200 kV.

Powder XRD patterns were recorded by using a Philips X'Pert Pro Super X-ray diffractometer with Cu-Kα radiation (λ = 1.5418 Å).

Nitrogen adsorption-desorption isotherms were measured with a Micromeritics ASAP 2020 adsorption apparatus at 77 K to 1 bar.

UV-vis-NIR diffuse reflectance spectra were recorded in the spectral region of 250-2500 nm with a Shimadzu SolidSpec-3700 spectrophotometer.

Room-temperature ESR spectra were collected using a JEOL JES-FA200 electron spin resonance spectrometer (298 K, 9.062 GHz).

**3. Detection of hydrogen peroxide ($H_2O_2$):**

Production of $H_2O_2$ was detected by a reported *N*,*N*-diethyl-p-phenylenediamine (DPD)/horseradish peroxidase (POD) method.[S1] Briefly, 0.1 g of DPD and 0.1 g of POD were firstly dissolved in 10 mL of $H_2O$, respectively, and were stored in dark at below 278 K before used. Then the $CH_3CN$ solution obtained after the light-driven catalytic aerobic coupling of benzylamine was added into 10 mL of $H_2O$, and the mixture was further extracted by ethyl acetate (EtOAc, 20 mL) three times to remove the organic compounds. Then 0.5 mL of aqueous solution and 0.5 mL of PBS buffer (pH = 7.4) were added into 4 mL of $H_2O$ followed by a 10-sec shake. After adding 10 μL of DPD and 10 μL of POD solution, the UV-vis spectra of the sample were collected using an Agilent Varien Cary 60 spectrophotometer.

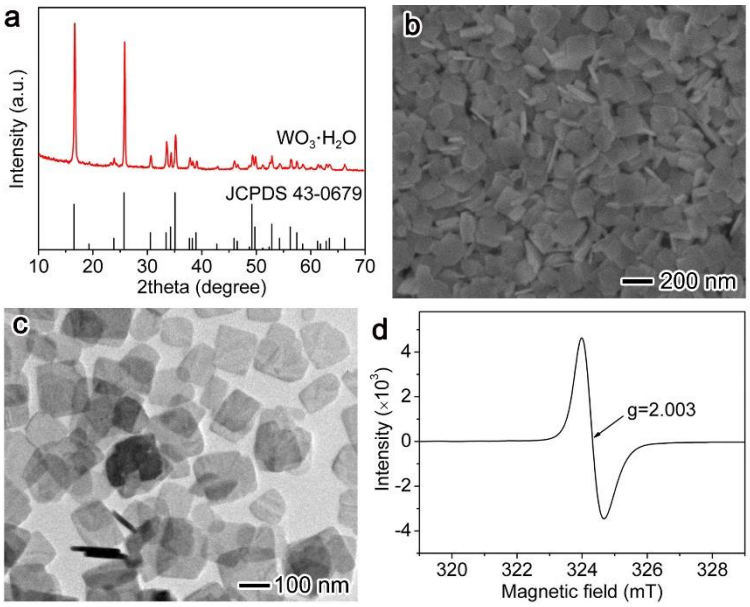


**Figure S1.** Characterization of the precursor of $WO_3 \cdot H_2O$ nanosheets. (a) XRD pattern. (b) SEM image. (c) TEM image. (d) Room-temperature ESR spectrum.

The defective green $WO_3 \cdot H_2O$ powder was synthesized through a mild hydrothermal method using $Na_2WO_4 \cdot 2H_2O$ as a tungsten source and glucose as a reductant. X-ray diffraction (XRD) peaks (Figure S1a) can be well assigned to $WO_3 \cdot H_2O$ (JCPDS No. 43-0679). The $WO_3 \cdot H_2O$ sample has a sheet-like morphology with an average edge length of 150 nm and thickness of 15 nm (Figure S1b and S1c). Benefiting from the introduction of reducing agent (i.e., glucose), the $WO_3 \cdot H_2O$ sample contains numerous defects, and exhibits a symmetrical signal at g = 2.003 in the ESR spectrum (Figure S1d) similarly to R-$WO_3$ (shown in Figure 1h).

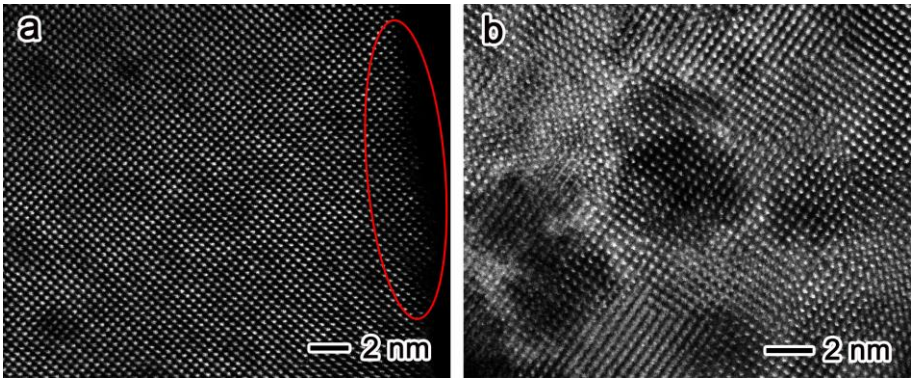


**Figure S2.** The additional atomic-resolution HAADF-STEM images of (a) D-$WO_3$ and (b) R-$WO_3$ samples.

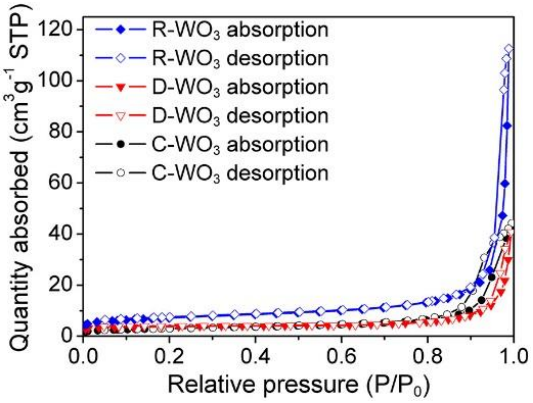


**Figure S3.** Nitrogen absorption-desorption isotherms of D-$WO_3$, R-$WO_3$ and C-$WO_3$ samples at 77 K.

According to the nitrogen absorption-desorption isotherm at 77 K (Figure S3), we can calculate the Brunauer-Emmett-Teller (BET) surface area as listed in Table S1. The larger BET surface area of R-$WO_3$ can be considered as the contribution from numerous small pits.

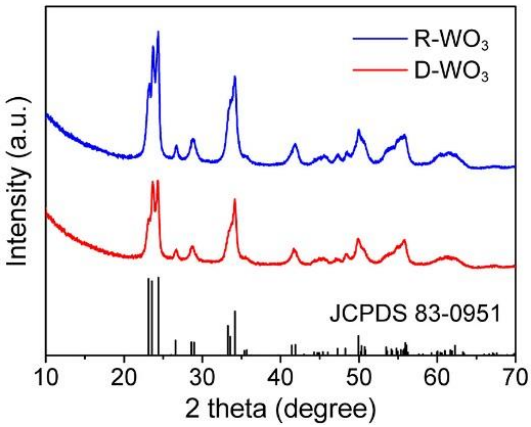


**Figure S4.** Powder XRD patterns of defect-controlled $WO_3$ nanosheets.

Despite their varied concentrations of oxygen vacancies, the XRD peaks for both R-$WO_3$ and D-$WO_3$ (Figure S4) can be well assigned to monoclinic $WO_3$ (JCPDS No. 83-0951).

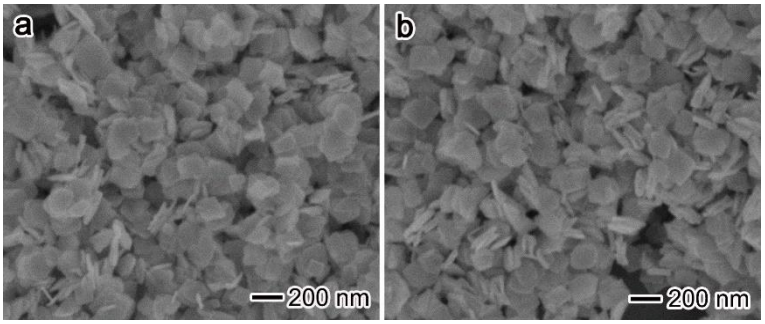


**Figure S5.** SEM images of (a) D-$WO_3$ and (b) R-$WO_3$ samples.

As indicated by scanning electron microscopy (SEM) (Figure S5) and transmission electron microscopy (TEM) images (Figures 1a and 1d), both R-$WO_3$ and D-$WO_3$ samples possess a sheet-like morphology, inherited from their precursor of $WO_3 \cdot H_2O$ nanosheets.

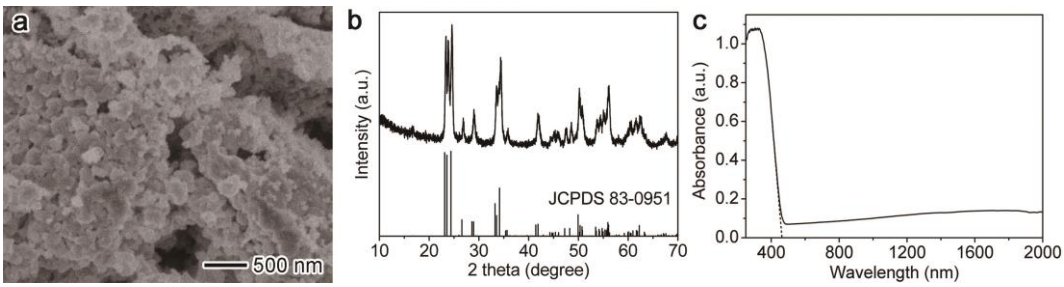


**Figure S6.** Characterization of commercial $WO_3$ (C-$WO_3$). (a) SEM image. (b) XRD pattern. (c) UV-vis diffuse reflectance spectrum.

As revealed by Figure S6a, the commercial $WO_3$ sample (C-$WO_3$) is nanocrystalline with particle sizes below 200 nm. In addition, the C-$WO_3$ has a monoclinic phase according to the XRD pattern (Figure S6b), and exhibits comparable light absorption to D-$WO_3$ (Figure S6c).

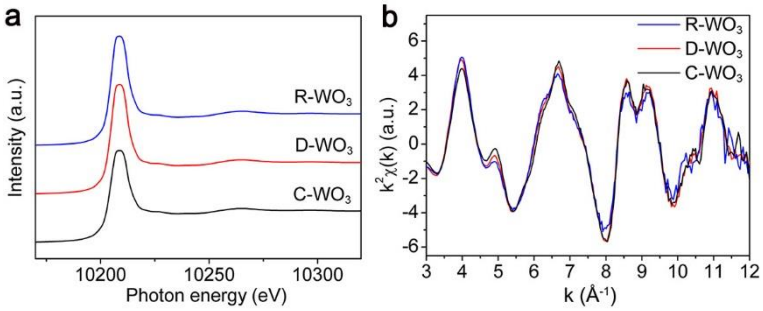


**Figure S7.** W $L_3$-edge X-ray absorption fine structure (XAFS) measurements for D-$WO_3$, R-$WO_3$ and C-$WO_3$ samples. (a) The normalized X-ray absorption near-edge structure (XANES) spectra. (b) W $L_3$-edge extended XAFS (EXAFS) oscillation function $k^2\chi(k)$.

The acquired EXAFS data were processed according to the standard procedures using the WinXAS 3.1 program.[S2] Theoretical amplitudes and phase-shift functions were calculated with the FEFF8.2 code using the crystal structural parameters of the $WO_3$ foil.[S3]

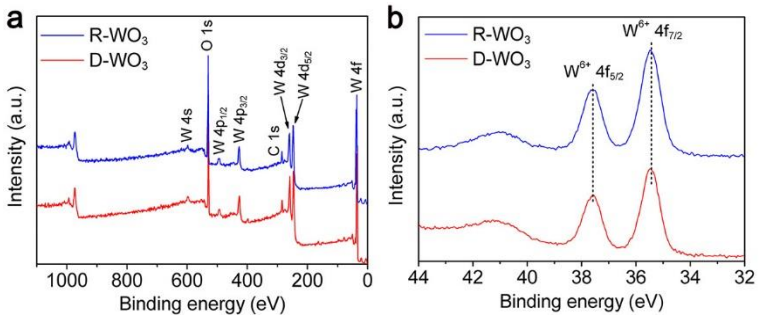


**Figure S8.** XPS spectra of D-$WO_3$ and R-$WO_3$ samples. (a) XPS survey spectra. (b) High-resolution W 4f spectra.

In the W 4f XPS spectra (Figure S8b), two peaks at binding energies of 35.4 and 37.6 eV corresponding to $4f_{7/2}$ and $4f_{5/2}$ of $W^{6+}$, respectively,[S4] have been detected for both D-$WO_3$ and R-$WO_3$. No peaks have been observed for $W^{5+}$ or $W^{4+}$.

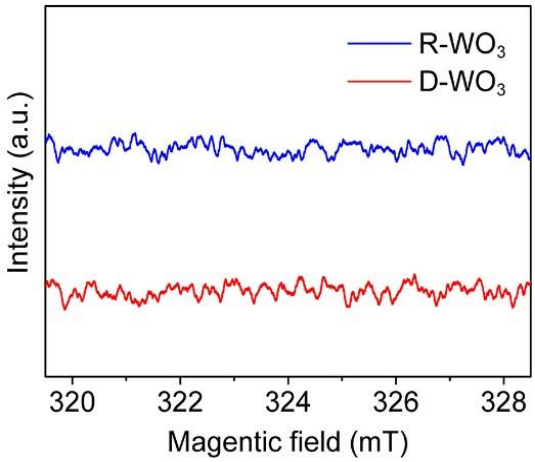


**Figure S9.** ESR detection of superoxide radicals using a DMPO spin-trapping agent. The methanol solution of DMPO was mixed with R-$WO_3$ or D-$WO_3$ in the dark.

Without light illumination, no quartet pattern for the $O_2^{\bullet-}$ captured by DMPO was observed in ESR spectra (Figure S9) regardless of the oxygen vacancy concentrations in $WO_3$.

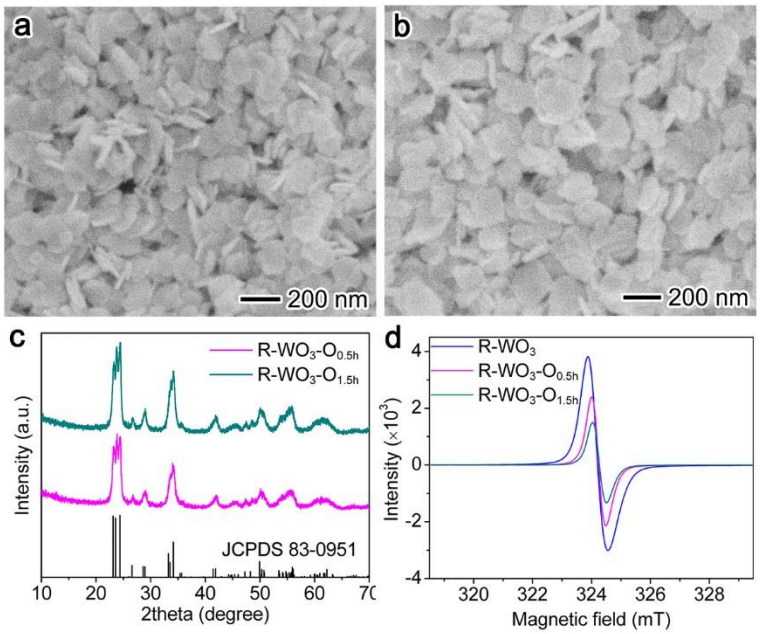


**Figure S10.** Characterization of the R-$WO_3$-$O_{0.5h}$ and R-$WO_3$-$O_{1.5h}$ that were prepared by re-calcining R-$WO_3$ at 623 K in the air for 0.5 h or 1.5 h, respectively. (a) SEM image of R-$WO_3$-$O_{0.5h}$. (b) SEM image of R-$WO_3$-$O_{1.5h}$. (c) XRD patterns. (d) Room-temperature ESR spectra.

As compared with R-$WO_3$, the morphology and crystal phase were well maintained after re-calcination (Figures S10a-c). However, the concentrations of oxygen vacancies were gradually reduced by increasing the re-calcination time, according to the signal intensities in ESR (Figure S10d).

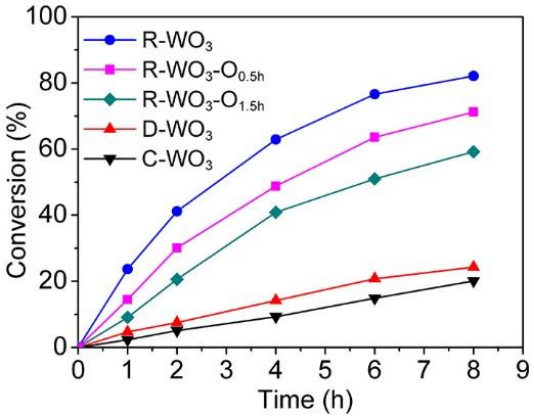


**Figure S11.** Time-dependent conversion yields for aerobic coupling of benzylamine by various catalysts. Reaction condition: benzylamine (0.1 mmol), catalyst (20 mg), solvent ($CH_3CN$, 4 mL), $O_2$ (1 atm), light ($\lambda$ > 400 nm, 100 mW $cm^{-2}$), temperature (298 K).

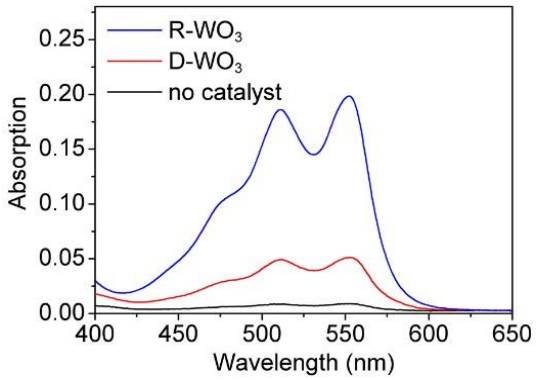


**Figure S12.** Detection of $H_2O_2$ for the solution after the light-driven catalytic aerobic coupling of benzylamine by R-$WO_3$ or D-$WO_3$ for 2 h, using a DPD/POD method.

According to the mechanism,[S1, S5] DPD can be oxidized by $H_2O_2$ to a higher valent state using POD as a catalyst. The radical cation ($DPD^{\cdot+}$) produced from the oxidation of two DPD molecules exhibits two absorption maxima at 510 and 551 nm. As a peroxidase, the POD well recognizes $H_2O_2$ and exhibits excellent selectivity for $H_2O_2$. Thus this method cannot only detect $H_2O_2$ but also distinguish it from other oxidants such as superoxide radicals. The process for the oxidation of DPD is shown as follows:

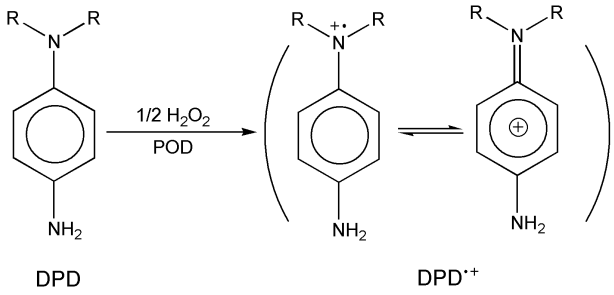


In our reaction system, the $H_2O_2$ intermediate has been observed based on these two absorption maxima in Figure S12.

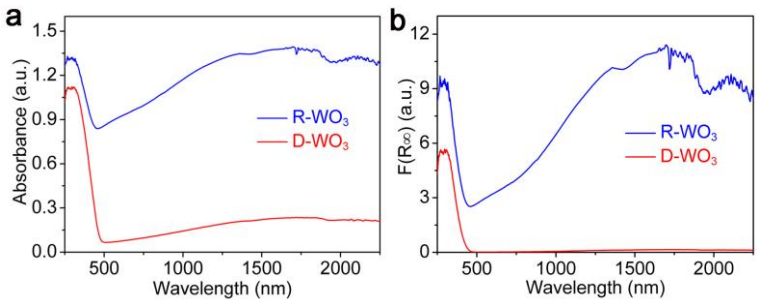


**Figure S13.** (a) UV-vis-IR diffuse reflectance spectra and (b) the converted Kubelka-Munk functions of D-$WO_3$ and R-$WO_3$.

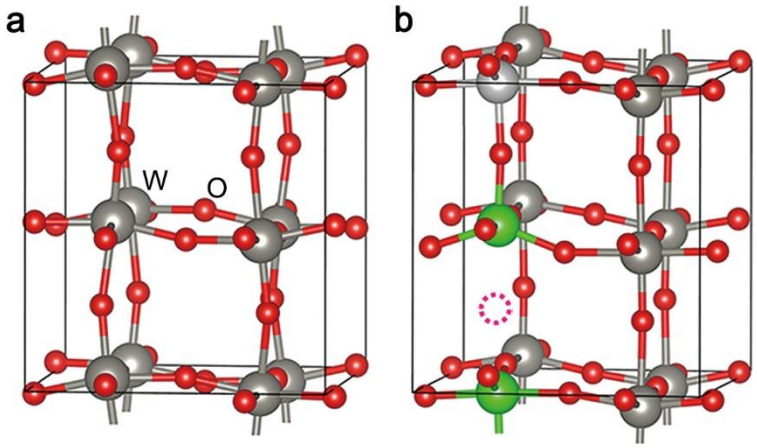


**Figure S14.** Structural models for the simulations on electronic band structures. (a) Perfect $WO_3$ lattice. (b) $WO_3$ lattice with an oxygen vacancy incorporated. The green beads represent the W atoms located at the oxygen vacancy.

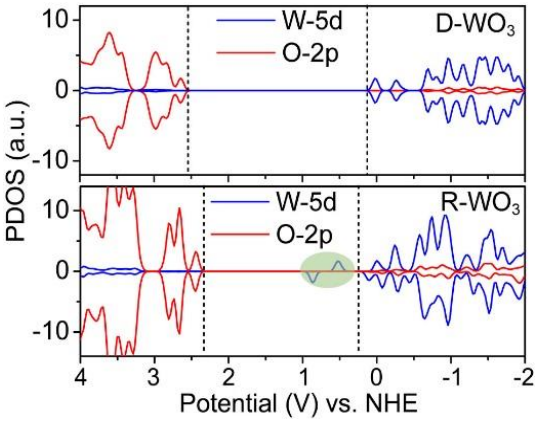


**Figure S15.** Partial DOS (PDOS) diagrams from first-principles calculations for perfect $WO_3$ (D-$WO_3$) and defective $WO_3$ (R-$WO_3$).

The computed partial densities of states (PDOS) diagrams (Figure S15) reveal that the conduction and valence band edges are primarily contributed by W 5d and O 2p orbitals, respectively. The unsaturated W atoms located at the oxygen vacancy donate electrons to O atoms,[S6] elevating the potential of O 2p orbitals. This change in O 2p moves up valence band maximum (VBM) to narrow bandgaps from 2.46 to 2.16 eV. Furthermore, the PDOS diagrams identify the emergence of defect states below conduction band minimum (CBM).


**Figure S16.** The photographs of D-$WO_3$ and R-$WO_3$ samples.

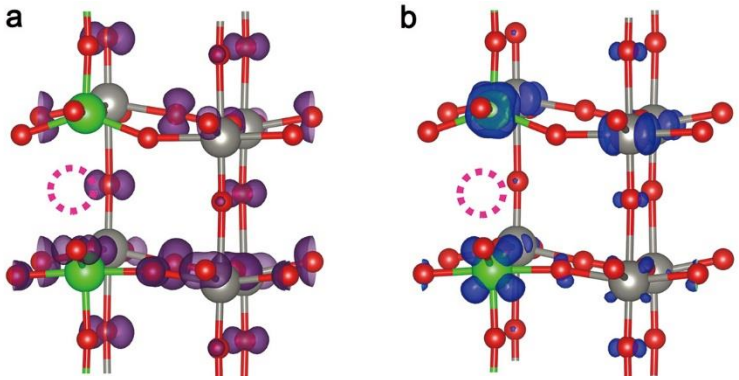


**Figure S17.** Wavefunction population in defective $WO_3$, obtained from first-principles calculations. (a) Valence band maximum (VBM). (b) Defect states below conduction band minimum (CBM). The green beads represent the W atoms with oxygen vacancies. The purple and blue color depicts the occupied and unoccupied wavefunction distribution, respectively.

The wavefunction of defect states below CBM mainly distributes on the W atoms with oxygen vacancies (Figure S17b), while that of VBM states is concentrated on those O atoms bonded to the neighbored W atoms (Figure S17a). It indicates that the photo-generated electrons and holes would be preferentially accumulated at the vacancy-located W atoms and at the O atoms bonded to the neighbored W atoms, respectively.

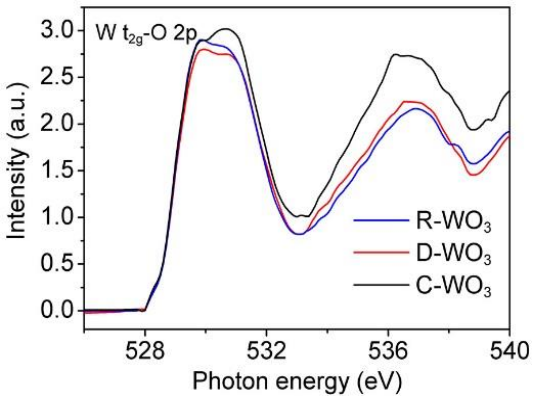


**Figure S18.** The normalized O *K*-edge NEXAFS spectra of D-$WO_3$, R-$WO_3$ and C-$WO_3$ samples. All spectra were normalized to the absorption edge jump.

O *K*-edge near-edge X-ray absorption fine structure (NEXAFS) spectroscopy can investigate the electronic structures of samples. In accordance with crystal-field theory, the W 5d orbitals in a $WO_6$ octahedron split into the $t_{2g}$-$e_g$ electronic configuration which is influenced by the coordination of lattice oxygen. As shown in Figure S18, the peak at ~530 eV corresponds to the electronic transition from 1s (O) to 5d-$t_{2g}$ (W) orbitals. Obviously this peak splits into two sub-peaks, originating from the distortion of $WO_6$ octahedron and the anisotropy of $t_{2g}$ band.[S7] According to the dipole selection rule, the O *K*-edge spectra show transitions from O 1s to the unoccupied states with p-character, which are relaxed due to the 1s core-hole positive charge.[S8] Thus the intensity of the peak is related to the degree of W-O bond covalency. In our case, the peak intensity of R-$WO_3$ is slightly higher than D-$WO_3$, indicating the enhancement of W-O bond covalency. The stronger W-O covalency where the W atoms have more O-2p character can promote the electron transfer between W atoms and adsorbates.[S9, S10]

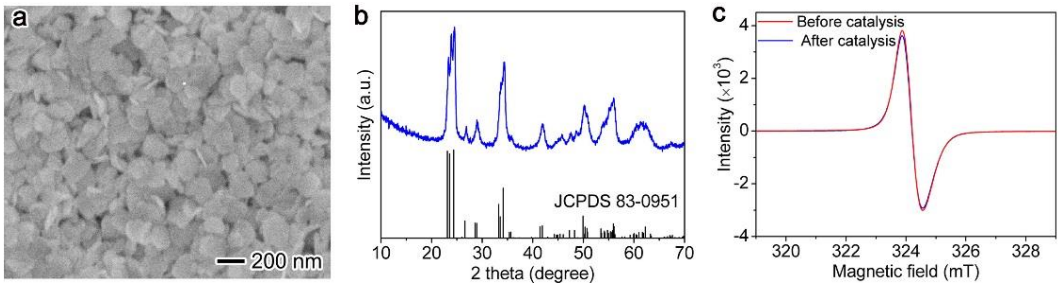


**Figure S19.** Characterization of the R-$WO_3$ sample after 6 catalytic cycles (i.e., the cyclic tests in main text, Figure 4a). (a) SEM image. (b) XRD pattern. (c) Room-temperature ESR spectra.

After 6 catalytic cycles up to 48 hours, the morphology (Figure S19a), crystal phase (Figure S19b), and vacancy concentration (Figure S19c) of R-$WO_3$ all were well maintained.

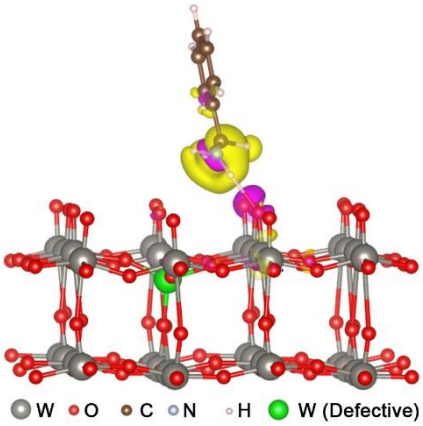


**Figure S20.** Differential charge density for the adsorbed benzylamine upon introducing a hole. The charge densities were simulated by first-principles calculations, and the purple and olive colors represent increase and decrease in electron density, respectively.

Looking into the distribution of hole charges in benzylamine (Figure S20), one can recognize that the C-H and N-H bonds are enriched with the transferred holes so as to promote the benzylamine activation.

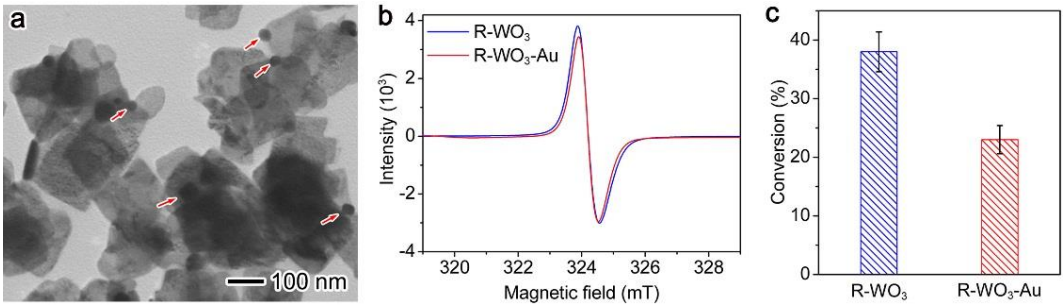


**Figure S21.** Characterization and catalytic performance of R-$WO_3$-Au hybrid structure. (a) TEM image (the locations of Au nanoparticles marked by red arrows). (b) Room-temperature ESR spectra. (c) Catalytic performance in aerobic coupling of benzylamine under irradiation of $\lambda > 400$ nm. Reaction time: 2h.

As displayed in Figure S21a, Au nanoparticles were deposited on the surface of R-$WO_3$ through photodeposition. With the deposition of Au nanoparticles, the oxygen vacancies were not diminished according to the ESR characterization (Figure S21b). The Au nanoparticles can trap the photo-generated electrons via the well-known Schottky junction. As a result, the efficiency of benzylamine oxidative coupling dramatically decreased (Figure S21c).

**Table S1.** BET surface areas of C-$WO_3$, D-$WO_3$, and R-$WO_3$ obtained from the data in Figure S3.

| Sample | C-$WO_3$ | D-$WO_3$ | R-$WO_3$ |
|---|---|---|---|
| BET surface area ($m^2$ $g^{-1}$) | 10.65 | 12.58 | 25.27 |

As shown in Table S1, the calculated BET surface area of D-$WO_3$ is 12.58 $m^2 \cdot g^{-1}$, comparable to commercial $WO_3$ (C-$WO_3$) (10.65 $m^2 \cdot g^{-1}$). In sharp contrast, the surface area of R-$WO_3$ is 25.27 $m^2 \cdot g^{-1}$, 2 times larger than that of D-$WO_3$. All the samples are nanocrystalline according to the electron microscopy observations (Figures S6a, 1a and 1d). Ruling out the influence of particle size and morphology, the higher surface area of R-$WO_3$ can be considered as the contribution from numerous small pits.

**Table S2.** Linear fitting results for the kinetic plots of light-driven catalytic aerobic coupling by various catalysts.

| Sample | Linear fitting equation | Adj. R-square | $k$ ($h^{-1}$) |
|---|---|---|---|
| R-$WO_3$ | y = 0.211t + 0.107 | 0.9857 | 0.211±0.012 |
| R-$WO_3$-$O_{0.5h}$ | y = 0.156t + 0.032 | 0.9927 | 0.156±0.007 |
| R-$WO_3$-$O_{1.5h}$ | y = 0.115t + 0.009 | 0.9837 | 0.115±0.007 |
| D-$WO_3$ | y = 0.034t + 0.015 | 0.9895 | 0.034±0.002 |
| C-$WO_3$ | y = 0.028t – 0.008 | 0.9944 | 0.028±0.001 |

Reaction condition: benzylamine (0.1 mmol), catalyst (20 mg), $O_2$ (1 atm), solvent ($CH_3CN$, 4 mL), light ($\lambda$ > 400 nm, 100 mW $cm^{-2}$), temperature (298 K).
y, $-\ln(c/c_0)$; t, reaction time.

The catalytic aerobic coupling of benzylamine to *N*-benzylbenzaldimine is regarded as a pseudo-first order reaction.[S11]

**Table S3.** Performance of various catalysts in thermally-driven aerobic coupling of benzylamine in the dark.

| Entry | Catalyst | Temperature (K) | Conversion (%) | Selectivity (%) |
|---|---|---|---|---|
| 1 | R-$WO_3$ | 298 | 3 | >99 |
| 2 | R-$WO_3$ | 333 | 11 | >99 |
| 3 | D-$WO_3$ | 298 | <1 | - |
| 4 | D-$WO_3$ | 333 | <1 | - |
| 5 | C-$WO_3$ | 298 | <1 | - |
| 6 | C-$WO_3$ | 333 | <1 | - |

Reaction condition: benzylamine (0.1 mmol), catalyst (20 mg), $O_2$ (1 atm), solvent ($CH_3CN$, 4 mL), reaction time (2 h).

The reaction yield relied on the presence of oxygen vacancies even in the dark (Table S3).

**Table S4.** Performance of R-$WO_3$ in aerobic coupling of benzylamine under light irradiation in various atmosphere at 1 atm.

| Entry | Atmosphere | Conversion (%) | Selectivity (%) |
|---|---|---|---|
| 1 | $O_2$ | 38 | >99 |
| 2 | Air | 26 | >99 |
| 3 | Ar | 5 | >99 |

Reaction condition: benzylamine (0.1 mmol), R-$WO_3$ (20 mg), solvent ($CH_3CN$, 4 mL), light ($\lambda$ > 400 nm, 100 mW $cm^{-2}$), temperature (298 K), reaction time (2 h).

The conversion yield depended on the concentration of $O_2$ in the reaction system (Table S4), indicating that the $O_2$ participated in the reaction.

**Supporting Note 1: further statement on the re-calcined R-$WO_3$ samples.**

The R-$WO_3$ was obtained by calcining the defective $WO_3 \cdot H_2O$ precursor at 673 K in the nitrogen atmosphere, and inherited the oxygen vacancies from the precursor. Owing to the high-temperature synthetic method, the oxygen vacancies remained in the R-$WO_3$ turned out to be very stable. As a matter of fact, the oxygen vacancies did not diminish even after calcining the R-$WO_3$ at 573 K in the air atmosphere for 1 h, which has been verified by the ESR spectra (Figure S22).

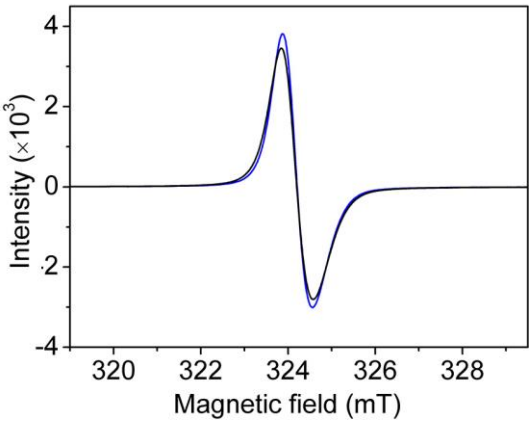


**Figure S22.** Room-temperature ESR spectra of the R-$WO_3$ (blue line) and the re-calcined R-$WO_3$ at 573 K for 1 h in the air atmosphere (black line).

To produce a set of samples with different concentrations of oxygen vacancies, we re-calcined the R-$WO_3$ in the air atmosphere at higher temperature 623 K (Figure S10). In this case, the oxygen vacancies could be partially filled with the oxygen in the air. Nevertheless, we have to point out that the oxygen vacancies gradually diminished during the calcination so their concentrations could be tailored by controlling the calcination time. As shown in Figure S10d, after calcining the R-$WO_3$ in the air for 30 min, the concentration of oxygen vacancies was obviously reduced. Prolonging the calcination time led to the further decrease in the concentration of oxygen vacancies. As a result, we could tailor the concentration of oxygen vacancies by varying the time for calcining R-$WO_3$ at 623 K in the air atmosphere. Note that too high calcination temperature (i.e., 673 K) significantly accelerated the rate of diminishing oxygen vacancies, making the process uncontrollable.

**Supporting Note 2: bandgap determination for D-$WO_3$ and R-$WO_3$**

It is well known that the Tauc plot is a widely used method for the determination of bandgaps.[S12,S13] Thus we determined the bandgaps of D-$WO_3$ and R-$WO_3$ using the Tauc plot according to the diffuse reflectance spectra. The Tauc equation is shown as follows:

$$(\alpha h\nu)^{1/n} = A(E_g - h\nu)$$

where α is the absorption coefficient, h is the Planck's constant, ν is the frequency of light, A is proportional constant, $E_g$ is bandgap, and n is equal to 2 as the transition is indirect for $WO_3$.[S14] According to the Kubelka-Munk theory, the Kubelka-Munk function ($F(R_\infty)$) for diffuse reflectance spectra is proportional to the absorption coefficient (α), which can be converted from the absorbance through the following equation:

$$R = 10^{-abs}$$

$$F(R_\infty) = (1-R_\infty^2)/2\ R_\infty$$

where abs is the absorbance of the light, and $R_\infty$ is relative reflectance. Thus the α in the Tauc equation can be substituted with $F(R_\infty)$.

$$(F(R_\infty)h\nu)^{1/2} = A(E_g - h\nu)$$

The diffuse reflectance spectra and the converted Kubelka-Munk functions are shown in Figure S13. Using the Kubelka-Munk function, the $(F(R_\infty)h\nu)^{1/2}$ is plotted against hν to determine the bandgaps (Figure 3a).

**References:**


S1. Bader, H.; Sturzenegger, V.; Hoigne, J. *Water Res.* **1988**, *22*, 1109−1115.

S2. Ressler, T. *J. Synchrotron Radiat.* **1998**, *5*, 118−122.

S3. Ankudinov, A.; Ravel, B.; Rehr, J.; Conradson, S. *Phys. Rev. B* **1998**, *58*, 7565−7576.

S4. Ho, S.-F.; Contarini, S.; Rabalais, J. *J. Phys. Chem.* **1987**, *91*, 4779−4788.

S5. Liang, S.; Wen, L.; Lin, S.; Bi, J.; Feng, P.; Fu, X.; Wu, L. *Angew. Chem. Int. Ed.* **2014**, *53*, 2951−2955.

S6. Naldoni, A.; Allieta, M.; Santangelo, S.; Marelli, M.; Fabbri, F.; Cappelli, S.; Bianchi, C. L.; Psaro, R.; Dal Santo, V. *J. Am. Chem. Soc.* **2012**, *134*, 7600−7603.

S7. Purans, J.; Kuzmin, A.; Parent, P.; Laffon, C. *Physica B* **1999**, *259*, 1157−1158.

S8. De Groot, F.; Grioni, M.; Fuggle, J.; Ghijsen, J.; Sawatzky, G.; Petersen, H. *Phys. Rev. B* **1989**, *40*, 5715−5723.

S9. Suntivich, J.; Gasteiger, H. A.; Yabuuchi, N.; Nakanishi, H.; Goodenough, J. B.; Shao-Horn, Y. *Nat. Chem.* **2011**, *3*, 546−550.

S10. Suntivich, J.; May, K. J.; Gasteiger, H. A.; Goodenough, J. B.; Shao-Horn, Y. *Science* **2011**, *334*, 1383−1385.

S11. Lang, X.; Ji, H.; Chen, C.; Ma, W.; Zhao, J. *Angew. Chem. Int. Ed.* **2011**, *50*, 3934−3937.

S12. Tauc, J.; Grigorovici, R.; Vancu, A. *Phys. Status. Solidi* **1966**, *15*, 627−637.

S13. Davis, E. A.; Mott, N. F. *Philos. Mag.* **1970**, *22*, 903−922.

S14. Su, J.; Feng, X.; Sloppy, J. D.; Guo, L.; Grimes, C. A. *Nano Lett.* **2011**, *11*, 203−208.